

REPORT DOCUMENTATION PAGE			Form Approved OMB NO. 0704-0188		
<p>The public reporting burden for this collection of information is estimated to average 1 hour per response, including the time for reviewing instructions, searching existing data sources, gathering and maintaining the data needed, and completing and reviewing the collection of information. Send comments regarding this burden estimate or any other aspect of this collection of information, including suggestions for reducing this burden, to Washington Headquarters Services, Directorate for Information Operations and Reports, 1215 Jefferson Davis Highway, Suite 1204, Arlington VA, 22202-4302. Respondents should be aware that notwithstanding any other provision of law, no person shall be subject to any penalty for failing to comply with a collection of information if it does not display a currently valid OMB control number.</p> <p>PLEASE DO NOT RETURN YOUR FORM TO THE ABOVE ADDRESS.</p>					
1. REPORT DATE (DD-MM-YYYY) 17-12-2014		2. REPORT TYPE Final Report		3. DATES COVERED (From - To) 1-Jul-2010 - 30-Jun-2011	
4. TITLE AND SUBTITLE Plamonics for Biomolecular Sensors and THz Metamaterial Waveguides Near and Far-Field Interfaces to DNA.Guided Nanostructures from RF to Lightwave:			5a. CONTRACT NUMBER W911NF-10-1-0229		
			5b. GRANT NUMBER		
			5c. PROGRAM ELEMENT NUMBER 622120		
6. AUTHORS Pinaki Mazumder			5d. PROJECT NUMBER		
			5e. TASK NUMBER		
			5f. WORK UNIT NUMBER		
7. PERFORMING ORGANIZATION NAMES AND ADDRESSES University of Michigan - Ann Arbor 3003 S. State St Ann Arbor, MI 48109 -1274			8. PERFORMING ORGANIZATION REPORT NUMBER		
9. SPONSORING/MONITORING AGENCY NAME(S) AND ADDRESS (ES) U.S. Army Research Office P.O. Box 12211 Research Triangle Park, NC 27709-2211			10. SPONSOR/MONITOR'S ACRONYM(S) ARO		
			11. SPONSOR/MONITOR'S REPORT NUMBER(S) 58176-EL.11		
12. DISTRIBUTION AVAILABILITY STATEMENT Approved for Public Release; Distribution Unlimited					
13. SUPPLEMENTARY NOTES The views, opinions and/or findings contained in this report are those of the author(s) and should not contrued as an official Department of the Army position, policy or decision, unless so designated by other documentation.					
14. ABSTRACT In THz frequencies, the textured surfaces on a subwavelength scale can support surface bound modes named spoofed surface plasmon polariton (SSPP) modes. Such modes mimic the common optical surface plasmon mode traveling at dielectric-metal interface, and therefore have similar mode profiles with strongly confined field and localized energy distribution. Specifically, when SSPP architectures are combined with dielectric loadings with distinctive material parameters, sample differentiation can be realized by tracking the shifted spectral output of the structure making it a good candidate for various sensing applications. Furthermore, SSPP concept can be applied to					
15. SUBJECT TERMS Terahertz, Biosensing, Mach Zehnder Interferometer, Multiplexer and Spoof surface Plasmon Polariton					
16. SECURITY CLASSIFICATION OF:			17. LIMITATION OF ABSTRACT UU	15. NUMBER OF PAGES	19a. NAME OF RESPONSIBLE PERSON Pinaki Mazumder
a. REPORT UU	b. ABSTRACT UU	c. THIS PAGE UU			19b. TELEPHONE NUMBER 734-763-2107

Report Title

Plamonics for Biomolecular Sensors and THz Metamaterial Waveguides

Near and Far-Field Interfaces to DNA-Guided Nanostructures from RF to Lightwave:
Exploiting the Spectrum for MURI-UCI

ABSTRACT

In THz frequencies, the textured surfaces on a subwavelength scale can support surface bound modes named spoofed surface plasmon polariton (SSPP) modes. Such modes mimic the common optical surface plasmon mode traveling at dielectric-metal interface, and therefore have similar mode profiles with strongly confined field and localized energy distribution. Specifically, when SSPP architectures are combined with dielectric loadings with distinctive material parameters, sample differentiation can be realized by tracking the shifted spectral output of the structure, making it a good candidate for various sensing applications. Furthermore, SSPP concept can be applied to various signal-processing components such as frequency selective filters and multiplexers.

Enter List of papers submitted or published that acknowledge ARO support from the start of the project to the date of this printing. List the papers, including journal references, in the following categories:

(a) Papers published in peer-reviewed journals (N/A for none)

Received

Paper

TOTAL:

Number of Papers published in peer-reviewed journals:

(b) Papers published in non-peer-reviewed journals (N/A for none)

Received

Paper

TOTAL:

Number of Papers published in non peer-reviewed journals:

(c) Presentations

Kyungjun Song, and Pinaki Mazumder, “Nonlinear Spoof Surface Plasmon Polariton Phenomena Based on Conductor Metamaterials,” Photon Nanostruct: Fundam Appl., July 2012

Zhao Xu, and Pinaki Mazumder, “Doubly Corrugated Spoofed Surface Plasmon Polariton (DC-SSPP) Structures With Frequency Selective Transmission,” Nanoelectronic Devices for Defense & Security Conference 2011, Polytechnic Institute of New York University, Brooklyn, New York

Zhao Xu, and Pinaki Mazumder, “Spoofed Surface Plasmon Mach-Zehnder Interferometer (MZI) Structure for THz Bio-Sensing Applications,” IEEE NANO 2012 - 12th International Conference on Nanotechnology, Birmingham, United Kingdom

Zhao Xu, Kyungjun Song and Pinaki Mazumder, “Analysis of Doubly Corrugated Spoof Surface Plasmon Polariton (DC-SSPP) Structure with Sub-Wavelength Transmission at THz Frequencies,” IEEE Transactions on Terahertz Science and Technology, Vol. 2, No. 3, pp 345-354, May 2012

Zhao Xu, and Pinaki Mazumder, “Bio-Sensing by Mach–Zehnder Interferometer Comprising Doubly-Corrugated Spoofed Surface Plasmon Polariton (DC-SSPP) Waveguide,” IEEE Transactions on Terahertz Science and Technology, Vol. 2, No. 4, pp 460-466, July 2012

Number of Presentations: 0.00

Non Peer-Reviewed Conference Proceeding publications (other than abstracts):

<u>Received</u>	<u>Paper</u>
-----------------	--------------

TOTAL:

Number of Non Peer-Reviewed Conference Proceeding publications (other than abstracts):

Peer-Reviewed Conference Proceeding publications (other than abstracts):

<u>Received</u>	<u>Paper</u>
-----------------	--------------

08/23/2013	6.00	Kyungjun Song, Pinaki Mazumder, Zhao Xu. Spoofed Surface Plasmon Polariton (SSPP) Gap Structure for HighSensitivity Bio-Sensing in THz, IEEE Nano 2013 Conference Proceedings. 06-AUG-13, . : ,
------------	------	---

08/23/2013	7.00	Zhao Xu, Pinaki Mazumder. Spoofed Surface Plasmon Mach-Zehnder Interferometer (MZI) Structure for THz Bio-Sensing Applications, IEEE Nano 2012 Conference. 07-AUG-12, . : ,
------------	------	---

TOTAL: **2**

Number of Peer-Reviewed Conference Proceeding publications (other than abstracts):

(d) Manuscripts

<u>Received</u>	<u>Paper</u>
08/09/2011	1.00 Z. Xu, K. Song and P. Mazumder,. Analysis of Doubly Corrugated Spoof Surface Plasmon-Polariton THz Waveguiding Structure with Frequency Selective Transmission, , IEEE Transactions on Microwave Theory and Techniques (08 2011)
08/09/2011	2.00 Pinaki Mazumder, Jack East. Plasmonics for Biomolecular Sensors and THz Metamaterial Waveguides - Continuation of ARO Report, Manuscript (08 2011)
08/11/2011	3.00 Pinaki Mazumder. ARO Progress Report, Report (08 2011)
08/11/2011	4.00 Pinaki Mazumder, Jack East. ARO Progress Report - Continuation, Report (08 2011)
08/11/2011	5.00 Pinaki Mazumder. ARO Presentation Materials, Slides (08 2011)
08/23/2013	8.00 Kyungjun Song, Pinaki Mazumder. Nonlinear spoof surface plasmon polariton phenomenon based on conductor metamaterials, Photonics and Nanostructures - Fundamentals and Applications (04 2012)
08/23/2013	9.00 Zhao Xu, Pinaki Mazumder. Bio-Sensing by Mach-Zehnder Interferometer Comprising Doubly-Corrugated Spoofed Surface Plasmon Polariton (DC-SSPP) Waveguide, IEEE TRANSACTIONS ON Terahertz Science and Technology (07 2012)
08/23/2013	10.00 Zhao Xu, Kyungjun Song, Pinaki Mazumder. Analysis of Doubly Corrugated Spoof Surface Plasmon Polariton (DC-SSPP) Structure With Sub-Wavelength Transmission at THz Frequencies, IEEE Transaction on Terahertz Science and Technology (05 2012)
TOTAL:	8

Number of Manuscripts:

Books

<u>Received</u>	<u>Book</u>
-----------------	-------------

TOTAL:

Received

Book Chapter

TOTAL:

Patents Submitted

MACH-ZEHNDER INTERFEROMETER HAVING A DOUBLY-CORRUGATED SPOOFED SURFACE PLASMON
POLARITON WAVEGUIDE

Patents Awarded

Awards

Fellow of AAAS

Fellow of IEEE

IEEE Distinguished Lecturer for Electron Devices Society

Graduate Students

<u>NAME</u>	<u>PERCENT SUPPORTED</u>	Discipline
Mahdi Aghadjani	0.00	
Xu Zhao	0.00	
Nan Zheng	0.00	
Jaeyoung Kim	0.00	
Barangi Mahmood	0.00	
Yalcin Yilmar	0.00	
FTE Equivalent:	0.00	
Total Number:	6	

Names of Post Doctorates

<u>NAME</u>	<u>PERCENT SUPPORTED</u>
Kyungjun Song	0.00
Ebong Idong	0.00
FTE Equivalent:	0.00
Total Number:	2

Names of Faculty Supported

<u>NAME</u>	<u>PERCENT SUPPORTED</u>	National Academy Member
Pinaki Mazumder	0.00	
FTE Equivalent:	0.00	
Total Number:	1	

Names of Under Graduate students supported

<u>NAME</u>	<u>PERCENT SUPPORTED</u>	Discipline
Jinal Shah	0.00	
FTE Equivalent:	0.00	
Total Number:	1	

Student Metrics

This section only applies to graduating undergraduates supported by this agreement in this reporting period

The number of undergraduates funded by this agreement who graduated during this period: 1.00

The number of undergraduates funded by this agreement who graduated during this period with a degree in science, mathematics, engineering, or technology fields:..... 1.00

The number of undergraduates funded by your agreement who graduated during this period and will continue to pursue a graduate or Ph.D. degree in science, mathematics, engineering, or technology fields:..... 1.00

Number of graduating undergraduates who achieved a 3.5 GPA to 4.0 (4.0 max scale):..... 0.00

Number of graduating undergraduates funded by a DoD funded Center of Excellence grant for Education, Research and Engineering:..... 0.00

The number of undergraduates funded by your agreement who graduated during this period and intend to work for the Department of Defense 0.00

The number of undergraduates funded by your agreement who graduated during this period and will receive scholarships or fellowships for further studies in science, mathematics, engineering or technology fields:..... 0.00

Names of Personnel receiving masters degrees

<u>NAME</u>
Liu Hao
Total Number: 1

Names of personnel receiving PHDs

<u>NAME</u>
Total Number:

Names of other research staff

<u>NAME</u>	<u>PERCENT SUPPORTED</u>
FTE Equivalent:	
Total Number:	

Sub Contractors (DD882)

Inventions (DD882)

Scientific Progress

Accomplishments:

- We have developed an analytical simulation method based on E-M theories, which can produce reasonably good result. Combined with commercial software, it helps us in the initial design stages of any SSPP waveguide structures
- We have designed and simulated a DC-SSPP based MZI structure and demonstrated its feasibility
- We have test-fabricated on an SOI wafer various DC-SSPP structures, and have demonstrated our ability to fabricate such structures with robustness and accuracy

Further work:

- Project I: THz device simulation: effect of the metal thickness and lossy materials
- In combination with fabrication process, we will determine the thickness of the metal deposition on our DC-SSPP devices. The goal is to select the thickness which is enough to sustain the SSPP modes while at the same time easy and robust to fabricate
- The impact of lossy metal as well as dielectric materials on device performance will be carefully studied
- Theoretical model as well as FDTD simulations using commercial software are projected in this task
- Project II: improvement of fabrication procedure
- Fabricate flanges on separate wafer to give more room for test structures
- Increase backing layer thickness on wafers
- Improve cleaning process
- Calibrate oxide etch for vertical walls
- Modify assembly using wafer to wafer bonding instead of individual assembly
- Project III: testing of the 270GHz devices
- Using standard 17mil*34mil port testing platforms, we can get the port parameters of the DC-SSPP devices, including its transmission spectrum
- The result of such test will be used to improve our device design and to optimize our fabrication procedure
- Project IV: fabrication and testing of THz domain structures
- It requires smaller feature size and better accuracy. Etch control, metal deposition and device bounding will be the main focus in this task
- Testing of such devices would require THz testing platforms.

Technology Transfer

A US patent has been submitted under the title: MACH-ZEHNDER INTERFEROMETER HAVING A DOUBLY-CORRUGATED SPOOFED SURFACE PLASMON POLARITON WAVEGUIDE

Attorney Docket No. 2115-005568/US/CPA

The disclosure relates generally to bio-sensing using an interferometer and, more particularly, a Mach-Zehnder Interferometer having a doubly-corrugated spoofed surface plasmon polariton waveguide.

ARO & MURI (UCI) Combined Final Report

Contract Number: W911NF-10-1-0229 & 2010-2514 (W911NF-11-1-0024)

Title: Plamonics for Biomolecular Sensors and THz Metamaterial Waveguides
(Near and Far-Field Interfaces to DNA.Guided Nanostructures from RF to Lightwave:
Exploiting the Spectrum)

Program Manager: Dr. William Clark Division Cheif Electronic Division

Principle Investigator: Prof. Pinaki Mazumder, University of Michigan

Motivation

Terahertz elements and devices designed to work in the frequency range of 0.1–10 THz have attracted enormous research activities in the past decade due to its potential use in applications such as astronomical remote sensing, tag-free bio-molecular detection, and monitoring of harmful chemicals. A major hurdle encountered by designers of THz logic components is how to realize low-loss and low-dispersion transmission of electromagnetic signals. One way to overcome the problem is to introduce periodic surface features such as holes, grooves, and dimples onto the material interface of the structure, which generates a special surface mode known as the Spoofed Surface Plasmon Polariton (SSPP). Spoofed Surface Plasmon Polariton (SSPP) is known as a pseudo-surface mode in THz frequencies that mimics the slow wave nature and localized E-M field distribution of the plasmon mode typically observed in optical domain.

A common issue in the design of THz components is to achieve better spectral selectivity in the form of sharper transmission peaks. Higher sensitivity to the structural change caused by external stimuli is also preferred in the design of sensors and active components alike.

A great number of macro-sized biomolecules demonstrates distinct dielectric properties in THz due to the multitude of collective vibrational modes of their complex molecular structure. Taking advantage of this phenomenon, we can realize the non-invasive, agent-free differentiation of these molecules using the doubly-corrugated SSPP architecture. This functionality of the SSPP sensor can be further enhanced when modification and multiplexing of the architecture is involved in the device design, resulting in the minimization of sample needed for successful detection.

Objective

- (1) Design, fabricate and test of new class of THz waveguides and plasmonic sensors
- (2) Enhance the sensitivity and differentiability of GHz-THz bio-sensors
- (3) Develop ultrafast and low-power GHz-THz devices

Task: The overall research project was in general divided into four different tasks as shown below:

Task 1: Analysis of Doubly Corrugated Spoof Surface Plasmon-Polariton (DC-SSPP) Structures and Bio-Sensing by Mach-Zehnder Interferometer Comprising

Task 2: SSPP DNA sensor with single-arm ‘gap’ structure or waveguide-cavity-waveguide (WCW)

Task 3: MZI SSPP Architecture in DNA Bio-Sensing: Lossy Scenarios

Task 4: Fabrication of the SSPP architecture using CMOS compatible nanofabrication technique and device testing

Task 1 : Analysis of Doubly Corrugated Spoof Surface Plasmon-Polariton (DC-SSPP) Structures and Bio-Sensing by Mach-Zehnder Interferometer Comprising

The Doubly Corrugated Spoofed Surface Plasmon Polariton (DC-SSPP) structures at THz is studied. Frequency selectivity of the proposed structures is illustrated. In our work, we introduce 1-D periodic grooves onto opposing metal-dielectric interfaces of a waveguide, forming a doubly-corrugated Spoof Surface Plasmon-Polariton (DC-SSPP) structure. Such structure is illustrated in Fig. 1.

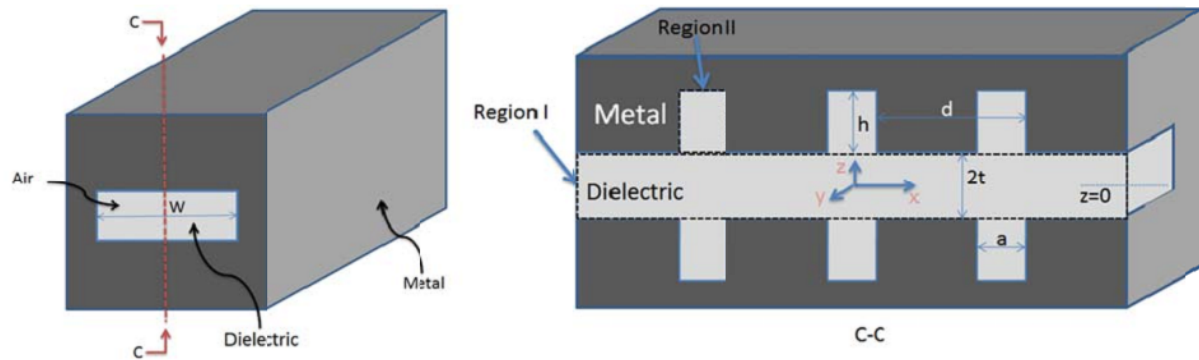


Fig. 1. (a) Front views of the SSPP structure (b) Cross section of the structure.

The structure is divided into two regions in order to derive the mathematical form of the dispersion relation. The 3-dimensional E-M fields are expressed in Region I and II. An eigenvalue equation can be obtained by enforcing the boundary conditions between the two regions, where the tangential fields must be continuous. In our previous study, we showed that such structure can support SSPP resonance mode, of which the dispersion relation is given by:

$$1 + \sum_{n=-\infty}^{\infty} \frac{k_{z,II}}{k_{z,I}^{(n)}} \frac{|T_n|^2}{\tan(k_{z,I}^{(n)} t)} \tan(k_{z,II} h) = 0 \quad (1)$$

Where

$$\begin{aligned}
|T_n|^2 &= \left| \sqrt{\frac{1}{ad}} \int_0^a e^{jk_{x,l}^{(n)} x} dx \right|^2 = \frac{a}{d} \left| \text{sinc} \left(\frac{k_{x,l}^{(n)}}{2} a \right) \right|^2 \\
v_y^2 &= k_0^2 - k_y^2 = \left(k_{x,l}^{(n)} \right)^2 + \left(k_{z,l}^{(n)} \right)^2 \text{ in Region I} \\
v_y^2 &= k_0^2 - k_y^2 = k_{x,II}^2 + k_{z,II}^2 \text{ in Region II, and} \\
k_y &= \frac{m\pi}{W}, m = 1, 2, \dots \\
k_{x,II} &= \frac{l\pi}{a}, l = 0, 1, 2, \dots
\end{aligned} \tag{2}$$

The dispersion relation of simple DC-SSPP structure, as calculated using the above formula, is shown in Fig. 2. It is shown that our SSPP waveguide has a unique band structure, where some modes demonstrate a near-zero group velocity. Those slow light modes are vital in achieving high Q-factor passing bands, which in turn, is highly desired property in the design of all sensors based on frequency finger-printing.

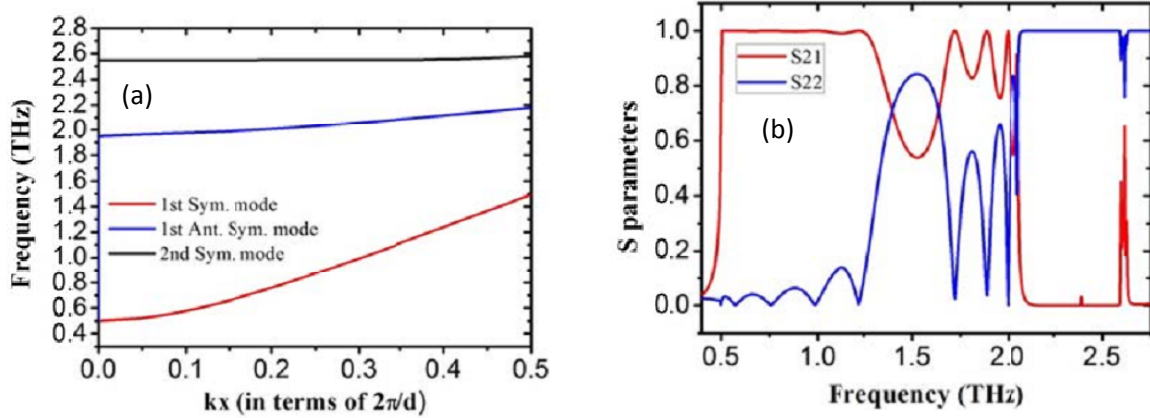


Fig. 2 (a) Dispersion diagram of sample DC-SSPP. (b) Transmission properties of DC-SSPP. Dimensions are:

$$d = 100\mu m, a = 10\mu m, h = 30\mu m, t = 33.33\mu m \text{ and } W = 300\mu m.$$

Fi.2 (b) shows the transmission properties of DC-SSPP in purpose of comparison with dispersion diagram. As shown, the results in both diagrams are in agreements.

The wave-vector is a function of refractive index n of the dielectric material. Therefore when a change of n is introduced, the phase accumulation of the THz wave travelling within the structure will be altered. As an example, the dispersion relationship of one DC-SSPP structure calculated from MATLAB is shown in Fig. 3 ($d = 100\mu m$, $a = 10\mu m$, $h = 80\mu m$, $t = 33.33\mu m$ and $W = 300\mu m$). The waveguide is made of dielectric materials having three different refractive indices $n_0 = 1$, $n_1 = 1.05$ and $n_2 = 1.15$. In the figure the dispersion curve is seen to be significantly lowered when higher refractive index material is used.

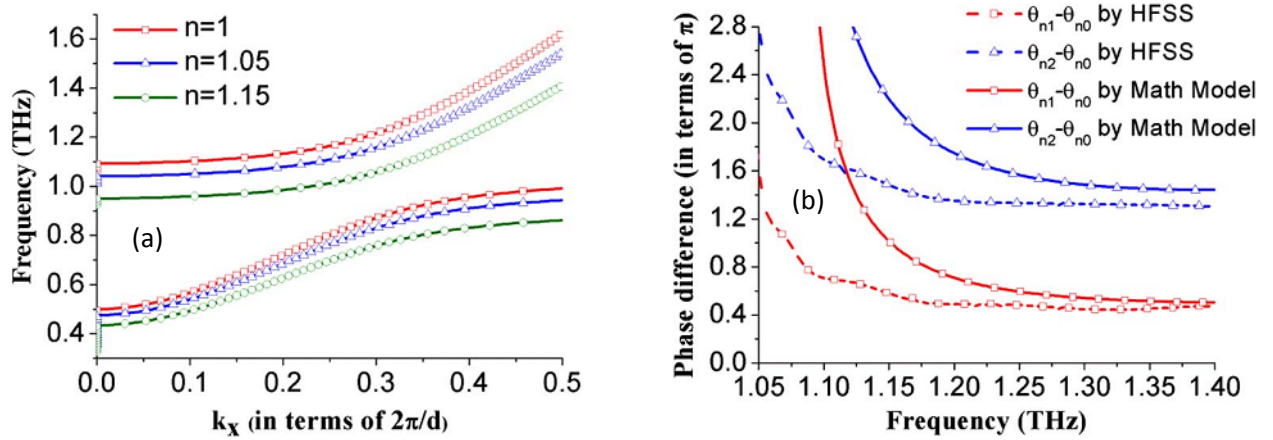


Fig. 3(a) Dispersion relation of the single-armed DC-SSPP structure when filled with dielectric material of different refractive indices. (b) Difference in phase accumulation for THz signals as a function of frequency between three refractive indices $n_0 = 1$, $n_1 = 1.05$ and $n_2 = 1.15$).

A natural result of this modified dispersion relations is the difference in phase accumulations when the THz signals propagate through such DC-SSPP structures with different dielectric constant. In Fig. 3(a) we show the phase difference of THz signals after it travels through seven periods of the DC-SSPP waveguide with three refractive indices ($n_0 = 1$, $n_1 = 1.05$ and $n_2 = 1.15$). The solid lines represent the result obtained from our mathematical model and the dashed lines show the simulation results obtained using HFSS. In Fig. 3(b) it is observed that the two curves are close to each other with frequencies far from the SSPP resonance. Near the band-gap region, despite the observable disparities, both curves show a sharp increase of the phase difference, as is predicted from Fig. 3 with flattened dispersion curves.

When phase modulation by changing refractive index is demonstrated as above, we can combine two arms of DC-SSPP waveguides to form an MZI (mach-zehnder interferometer). The THz signal from two arms of the MZI, when recombined after they propagate through different dielectric materials will be either enhanced or reduced in magnitude as a result of coherent interference. The combined effect of the selectivity of single-armed DC-SSPP waveguide and that of the interferometer will result in a transmission curve with sharper features as well as better sensitivity to structural variations caused by external modulations.

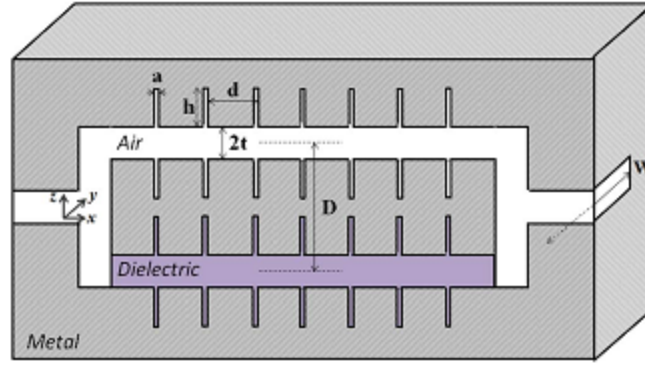


Fig. 4 Cross section of the DC-SSPP MZI structure with different geometric dimensions labeled. W is the width of the waveguide along the x -direction. The lower arm of the MZI structure (shaded in purple) designates the volume with dielectric loading.

In order to verify our idea, we have simulated the DC-SSPP MZI structure as depicted in Fig. 4. Various dimensions are labeled in the figure, with d denoting the distance between the two waveguide arms. The first structure we simulate has the dimensions of $d = 100\mu\text{m}$, $a = 10\mu\text{m}$, $h = 80\mu\text{m}$, $t = 33.33\mu\text{m}$, $W = 300\mu\text{m}$, and $D = 250\mu\text{m}$ each arm consists of a DC-SSPP waveguide with 7 grooves. With three different dielectric materials filling up one of the arms and air filling up the rest of the structure, the transmission curves of the MZI are shown in Fig. 5(a). For comparison, the transmission curves of the single arm DC-SSPP structure of the same dimensions are shown in Fig. 5(b).

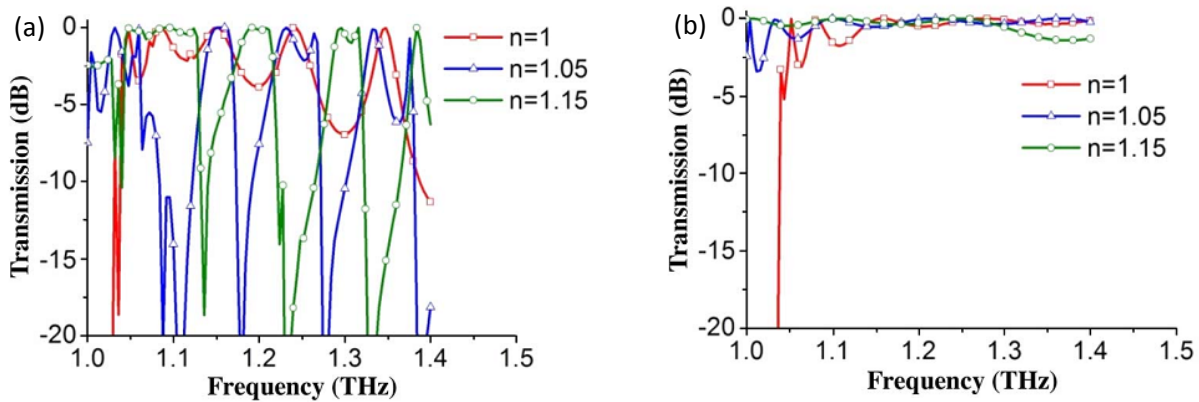


Fig. 5. Transmission spectrum of (a) the DC-SSPP MZI structure and (b) the single-armed DC-SSPP structure. Three different refractive indices are selected for the dielectric loading, and for MZI structure such loading only applies to one of the arms as depicted in Fig. 4.

By correlating the transmission with the phase difference, it is observed that significant suppression of the THz signal tends to happen when the phase difference between two arms of the interferometer is close to odd numbers of π . In Fig. 6, we have included the field distributions on the cross section of the structure at the frequency of THz. The constructive/destructive interference between the two arms in difference cases can be clearly

seen. It is noticed that for frequencies close to the SSPP resonance, the $-$ field is greatly localized in the groove region of the structure. It is consistent with the theoretical analysis we did before, where a strongly confined energy distribution of the THz wave is predicted near resonance. This property indicates the possibility of using less amount of dielectric loading to achieve the same selectivity of the structure.

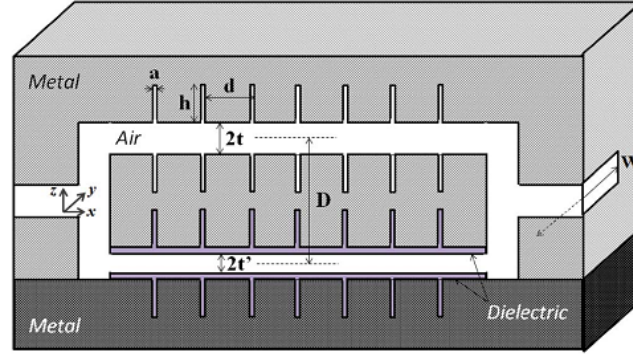
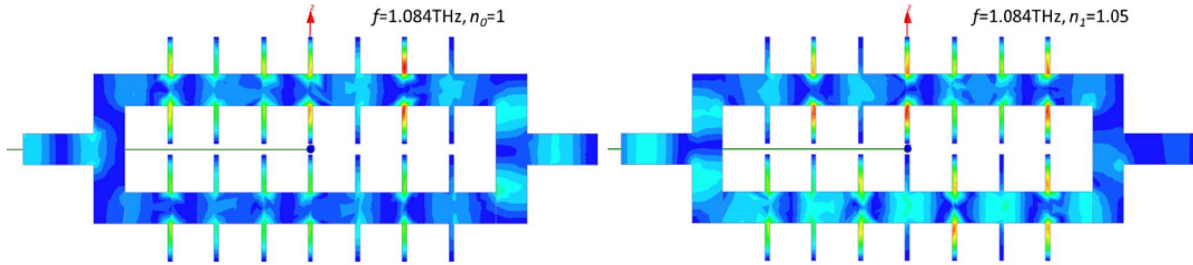


Fig. 6 Cross section of the DC-SSPP MZI structure with different geometric dimensions labeled. W is the width of the waveguide along the y –direction. Localized DNA loading is depicted as purple-shaded area in the sketch. The dark and light grey coloring of the metal part is merely to show the modular design of the sensor.

In Fig. 7 (a) shows example of field distribution in the DC-SSPP MZI structure at frequency of $f=1.084\text{THz}$ for two different refractive indices (magnitude of the overall field is plotted) $n_0 = 1$ and $n_1 = 1.05$. Fig. 7(b) illustrate the transmission spectrum of DC-SSPP MZI structure with partial loading inside the grooves for different refractive indices.



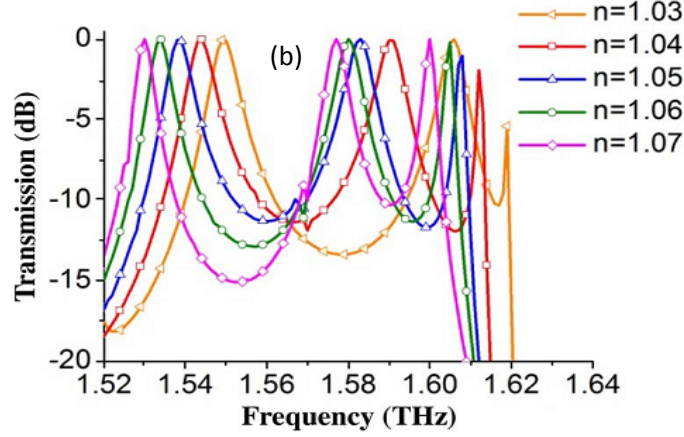


Fig. 7 (a) An example of field distribution in the DC-SSPP MZI structure at $f=1.084\text{THz}$ for two different refractive indices (magnitude of the overall field is plotted). The different dielectric loadings and frequencies are labeled on the upper right corner of each plot (b) Transmission spectrum of DC-SSPP MZI structure with partial loading inside the grooves.

Task 2: SSPP DNA sensor with single-arm ‘gap’ structure or waveguide-cavity-waveguide (WCW)

Despite the phase modulation of the propagating THz waves, in a periodic SSPP structure such modulation is induced by a refractive index change to the entire dielectric waveguide. This is however very unlikely in real bio-sensing scenarios. The large amount of sample needed in this case is contradictory to the goal of achieving better detection limit. Moreover, it is usually hard to implement given the limited sample volume provided by the molecular immobilization process. To overcome this problem, we introduce a gap structure into the SSPP waveguide, as shown in Fig. 8.

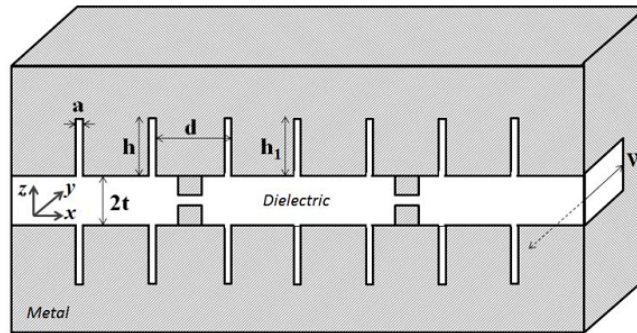


Fig. 8 Cross-section of the modified SSPP structure with gap blocks.

As shown, the structure consisting of two parts: cavity and waveguide. The structure can be regarded as equally spaced resonator array. The resonators in the waveguide are coupled at ω_w , and the coupled frequency for the cavity's resonators is ω_c . When the resonant frequencies of both parts are the same, the EM wave can couple from the waveguide to cavity and vice versa. Then to obtain the highest transmission in the switch it is essential that ω_w and ω_c coincide.

Using temporal coupled-wave analysis, the transmission and reflection of (waveguide-cavity-

waveguide) WCW structure can be described as:

$$T(\omega) = \frac{\Gamma_c^2}{(\omega - \omega_0)^2 + \Gamma_c^2}$$

$$R(\omega) = \frac{(\omega - \omega_0)^2}{(\omega - \omega_0)^2 + \Gamma_c^2}$$
(3)

And Γ_c can be described using:

$$\Gamma_c = \frac{\omega_0}{2Q}$$
(4)

At first we investigate the effect of change in real part of refractive index, then in (3) the cavity decay rate (Γ_0) is assumed to be zero. Which means no loss is assumed in the cavity. Based on (3) when the operating frequency is far from resonant frequency compared to Γ_c , ($|\omega - \omega_0| \gg \Gamma_c$) all the power will be reflected back. When the operation frequency is close to the cavity's resonant frequency ($|\omega - \omega_0| \ll \Gamma_c$) the transmission in (3) is approximately.

Fig. 9 shows the transmittance of the structure with different block dimensions. In the context of bio-sensing, refractive index n is the primary variable to be sensed. It is therefore chosen to be the x-axis of the plot throughout this paper in order to better illustrate the functionality of our structure. The probe signal frequency is chosen to be $f=1.08\text{THz}$ so that it is close to the band gap. The dimensions of the structure are $d = 100\mu\text{m}$, $a/d = 0.1$, $h/d = 0.8$, $h/h_2 = 1.05$, $t/d = 0.3$, and $W = 300\mu\text{m}$ so that the transmission peak is located at $n=1$, which mimics the case of air filling.

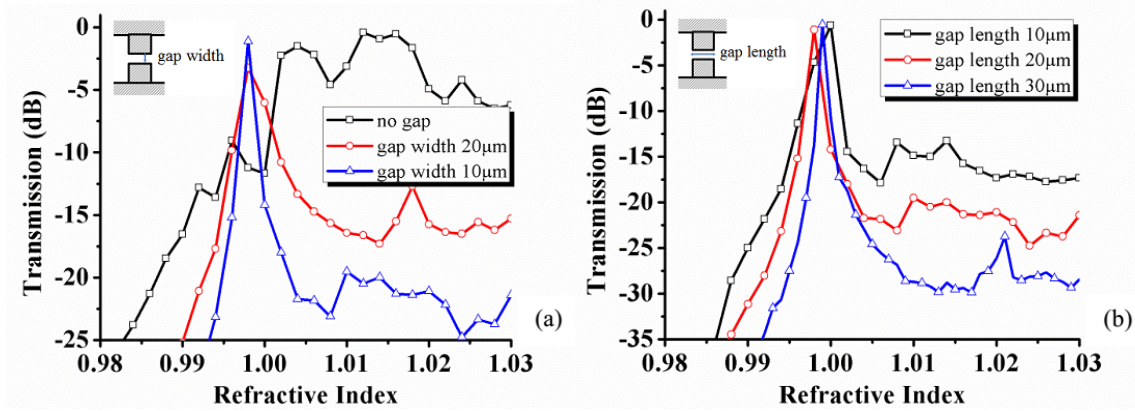


Fig. 9 Transmission of gapped SSPP structure as a function of sample refractive index at $f=1.08\text{THz}$, (a) with different gap widths, and (b) with different gap lengths.

The increased quality factor of the transmission peaks indicates the possibility of reducing the sample amount needed for successful detection. This is investigated by changing the sample loading pattern as shown in Fig. 10. SSPP architecture is known to have highly concentrated E-M field inside the groove region when it is close to resonance. As a result, sample deposition patterns that are localized inside the groove are used to compare with the fully loaded case. The four different patterns are denoted by: A) sample fully loaded; B) sample in groove volume only; C) thin layers of $2\mu\text{m}$ thickness on the groove wall and D) thin layers of $1\mu\text{m}$ thickness on the groove wall.

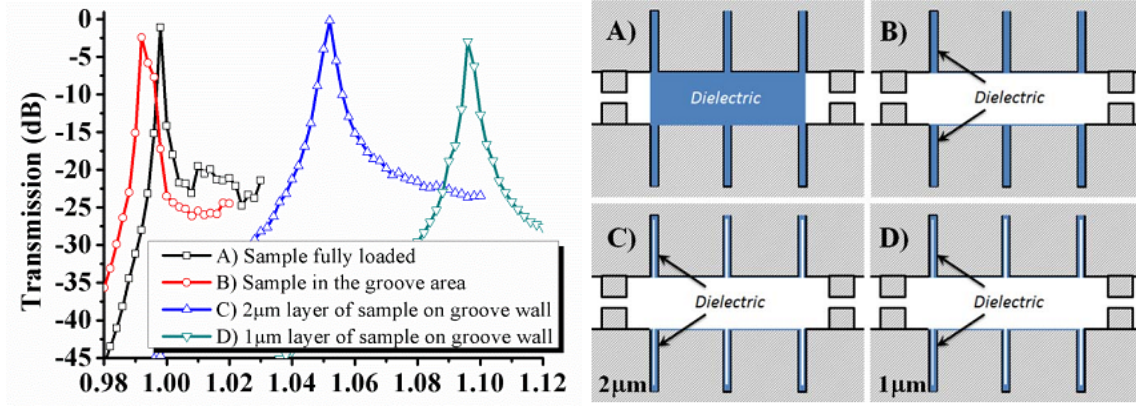


Fig. 10 Transmission of gapped SSPP structure as a function of sample refractive index with different sample deposition patterns

DNA sensing is therefore realized with localized sample deposition in the gapped SSPP architecture. This is illustrated in Fig. 10, where the transmission peak, in the case of the sample load pattern D), is plotted as a function of probe THz frequency. High transmission can be achieved for a wide range of refractive index from $n = 1.15$ to $n = 0.97$, corresponding to the frequency change from $f=1.073\text{THz}$ to $f=1.095\text{THz}$. It covers the n values for both denatured ($n = 1.05$) and hybridized DNA molecules ($n = 1.15$).

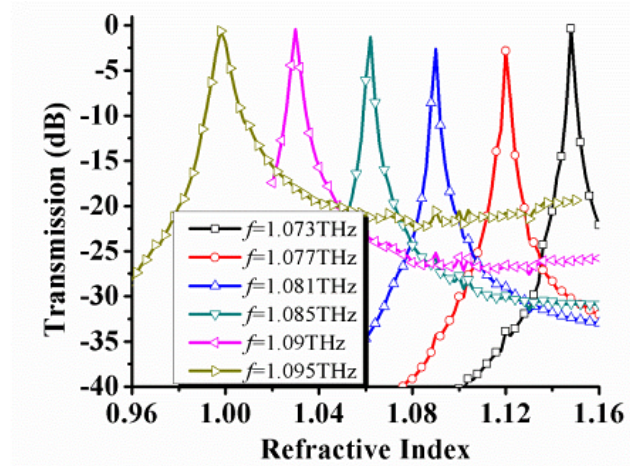


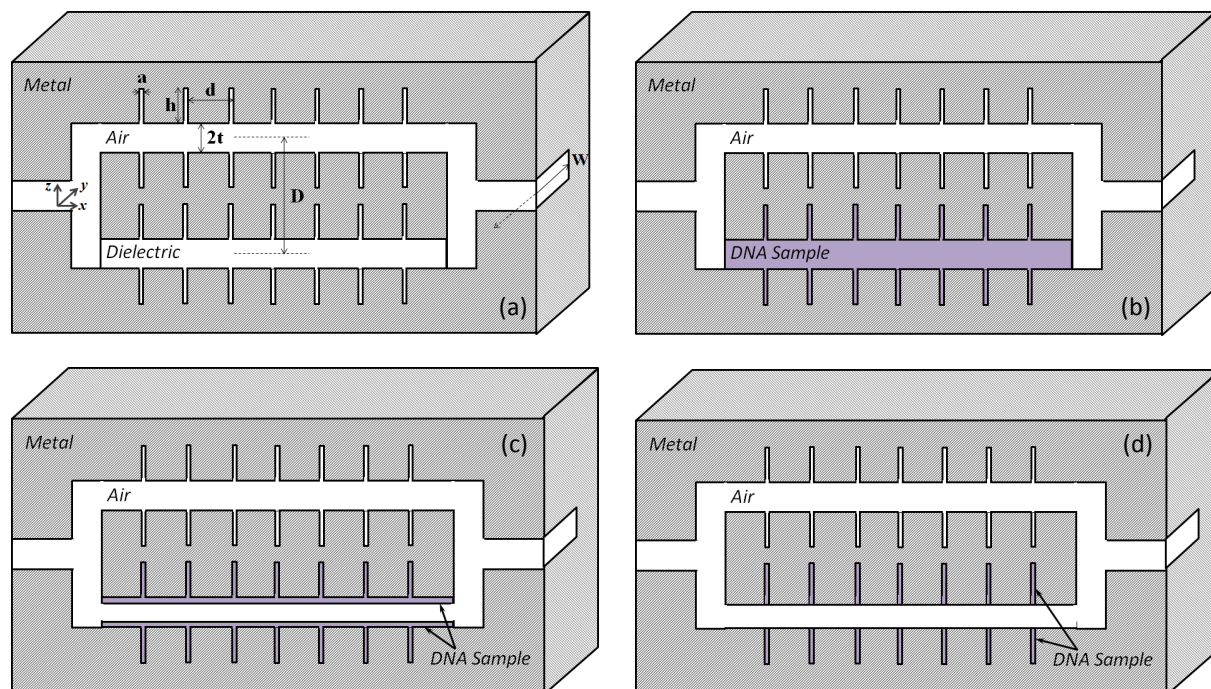
Fig. 11 Transmission of gapped SSPP structure as a function of sample refractive index at different probe frequencies with sample load pattern D)

Task 3: MZI SSPP Architecture in DNA Bio-Sensing: Lossy Scenarios

The dielectric response of the bio-molecules in these frequencies can be in general described using the following formula:

$$\varepsilon(\omega) = \varepsilon_0 + \int \frac{f(\omega')g(\omega')}{(\omega'^2 - \omega^2) + i\gamma(\omega')\omega} d\omega' + \varepsilon_r \int_0^\infty \frac{h(\tau)}{1 + i\omega\tau} d\tau \quad (5)$$

In (5), the second term represents the contribution from harmonic oscillations. Such modes can rise from translational, rotational or vibrational resonances of the molecular structure, and is strongly affected by the chemical composition and conformational shape of molecules. The third term, on the other hand, indicates the effect of inelastic relaxation. Water, for example, has a wide Debye relaxation peak in the THz frequencies, therefore is a significant contributor to this term should it exists in the sample of interest.



In case (b), the spectral output of the sensing architecture is shown in Fig. 5. When compared with the ideal case where no imaginary part of the refractive index is considered, the transmission peaks in this case is visibly lowered due to the material absorption. The differentiation between the curves of denatured and hybridized DNA is not pronounced when the frequency is far from the resonance. However, such differentiation is clearly observed close to such resonance, where peaks are located at distinct frequencies with extinction ratio reaching and even far exceeding 10dB.

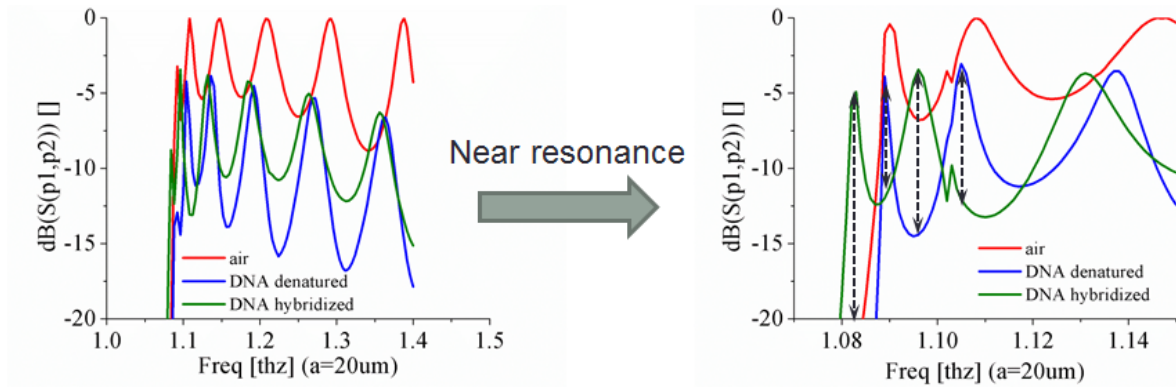


Fig. 13 Spectral response of the MZI SSPP sensing architecture with different samples filling up one arm

In case (c) and (d), the lowering of the transmission curves are alleviated due to smaller amount of sample used (Fig. 14 and 15). Similarly, when far from resonance, the spectral output of different DNA samples is mostly identical to each other. However, close to the band gap the distinct transmission peaks remain, even with a minimum amount of sample forming only a thin layer on the groove walls. In case (d) such effect may not be as pronounced as those in the other two cases, however further study can be done so that an optimal point between the sample usage, the detectability and the overall loss can be achieved.

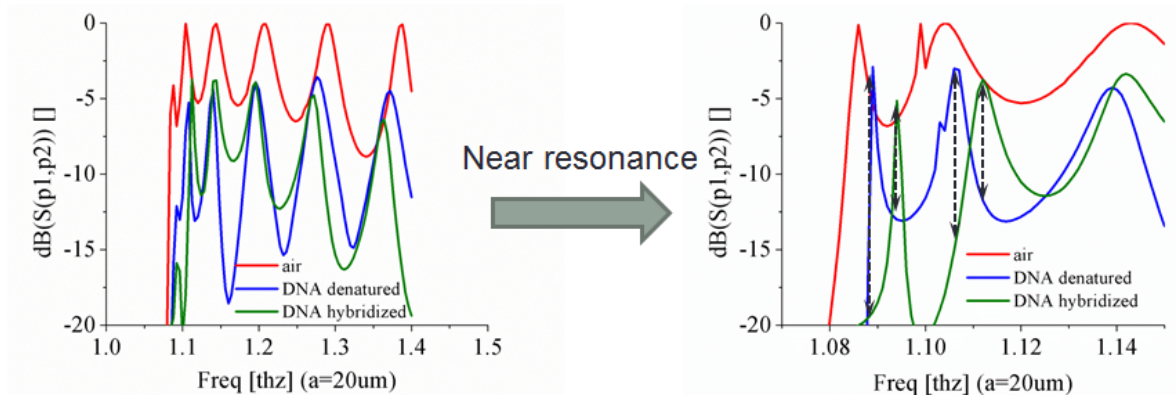


Fig.4 Spectral response of the MZI SSPP sensing architecture with different samples forming a thin layer on the opposing walls of one arm

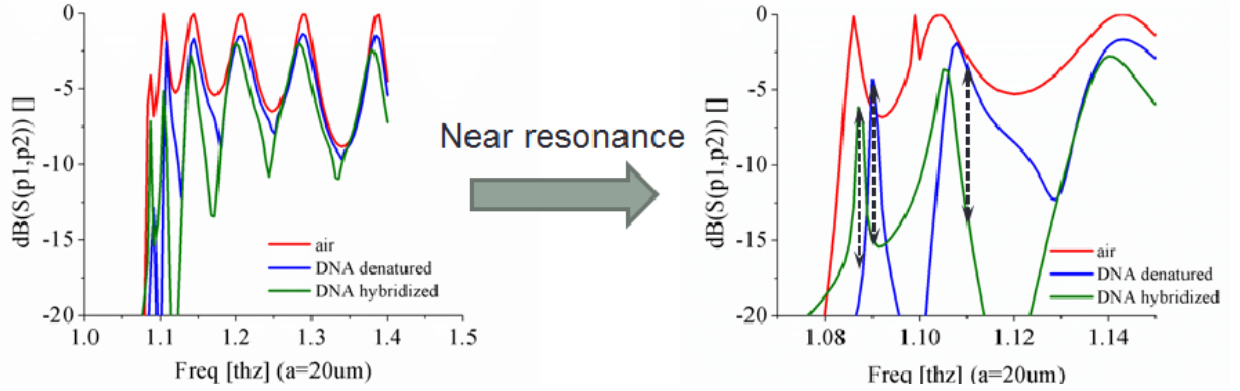


Fig.15 Spectral response of the MZI SSPP sensing architecture with different samples forming a thin layer on the walls of the groove area only

Similarly, we perform the simulation on DNA samples with hydration, using the assumption we mentioned in the previous section. The results are shown in Fig. 8. The loss tangent of water is orders of magnitude larger than that of dry DNA samples. It has resulted in great absorption loss even with the minimal sample loading and poor differentiability between the denatured and hybridized DNA samples. Our SSPP sensing architecture as is cannot be utilized to sense hydrated samples or DNA in solutions. Further study in modified designs is required if samples of such nature or *in-vivo* sensing is required in the long-term goal of this project.

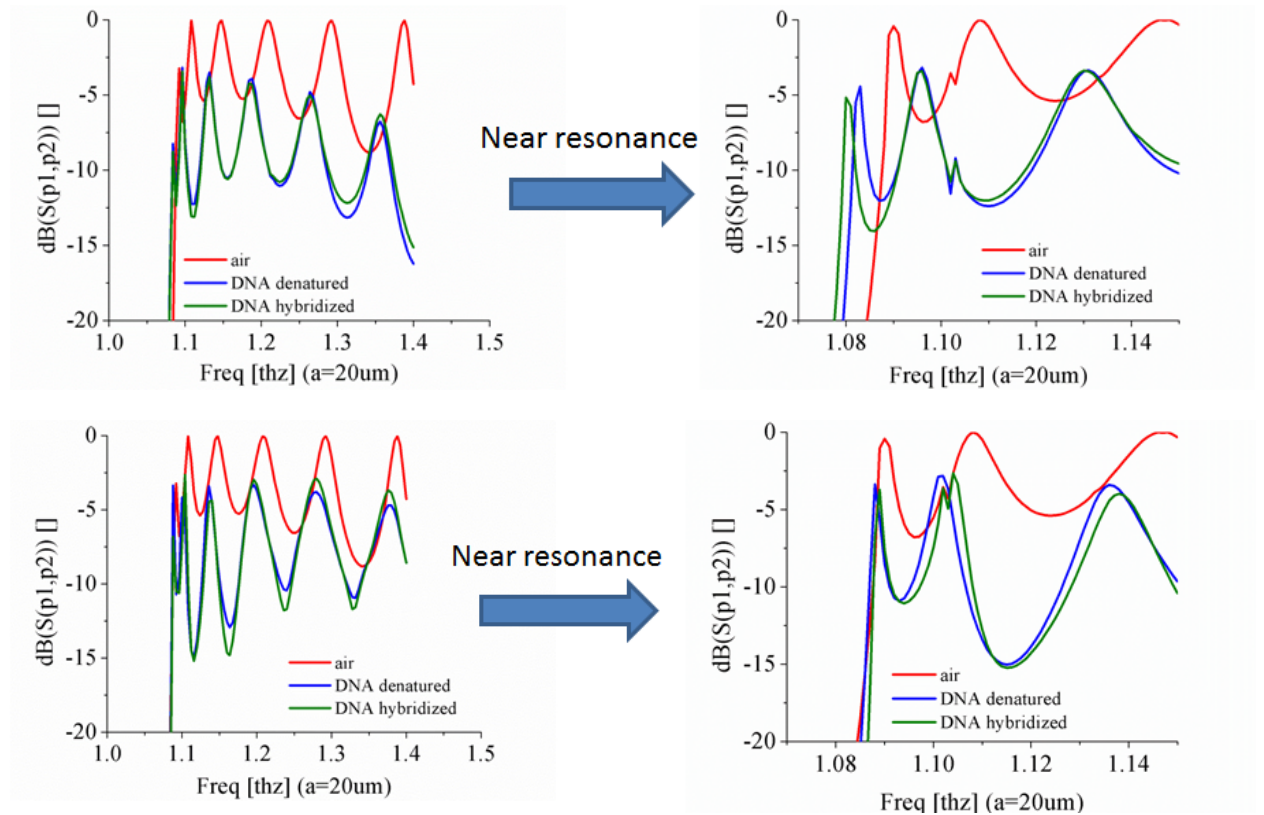


Fig. 16 Spectral response of the MZI SSPP sensing architecture assuming water absorption: (a) with different samples filling up one arm, and (b) with different samples forming a thin layer on the walls of the groove area only

Finally the simulations show that dry DNA samples with complex refractive index are incorporated into our model to count for intrinsic absorption loss. With non-zero loss factor, the transmission curves are lowered in general. The scale of such lowering is dependent on the exact sample loading pattern. While the differentiation of transmission peaks away from the SSPP resonance is mostly missing due to the absorption loss, there is still considerable distinction of those peaks between the two types of DNAs close to the bandgap, even with localized sample deposition. The loss of water is orders of magnitude higher than the intrinsic loss of dry DNA molecules. In simulation this has resulted in little difference between the transmission curves of the two samples.

Task 3: THZ Bio-Sensor Design II: De-/Multiplexer (De-/MUX)

We have shown that the DC-SSPP has stop and band passes range that can be tuned by changing the refractive index inside the waveguide. Using this property of DC-SSPP we can build Multiplexer/Demultiplexer. Fig. 17 shows the overall view of the structure. It is consisting of multiple arms enables parallel sensing of multiple samples at the same time. Enhanced selectivity enables localized sample usage. Using different biomaterial in each arm set the passing band of each arm at a certain frequency. Then the input signal based on its frequency passes through an arm that its passing frequency coincides with it. Finally, The difference in passing bands of separate arms of the De-/MUX structure can enhance the quality factor of the respective transmission peak. Our simulations show that $\frac{\Delta n}{n} = 0.0125$ is detectable with sample deposition only on the groove walls.

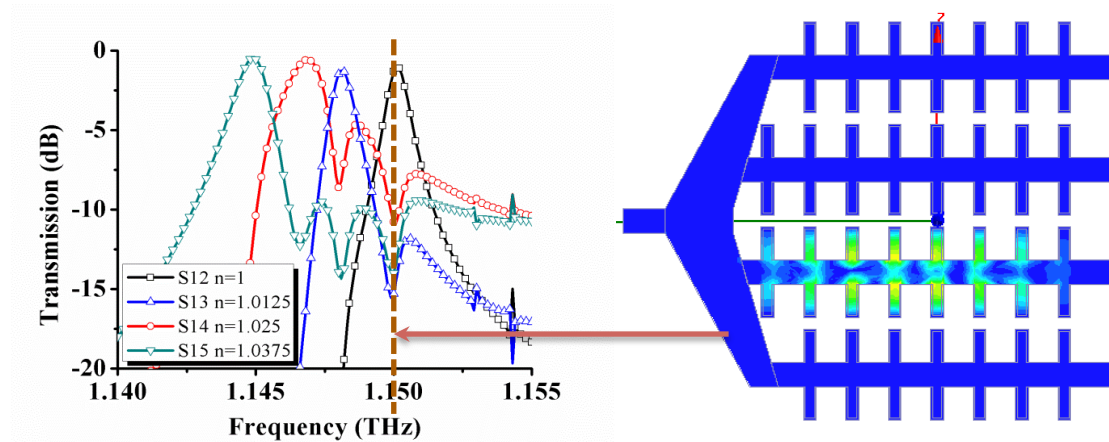


Fig. 17 Schematic view of Multiplexer/Demultiplexer consisting of multiple arms

Task 4: Fabrication of DC-SSPP structure

1. Fabrication Process:

Different geometric dimensions of the SSPP architecture have been included in the simulation and the later mask design, in order to test the structure performance as a function of dimension variations. Fig. 18 shows schematic view of a sample component that is fabricated, with the input and output ports designed using WR-3 standard (0.431mm by 0.863mm). As can be seen, it has feature dimensions as small as $180\mu\text{m}$. The fabrication process is two masks process and consists of four major steps:

1. Spinning, exposing, developing, and patterning top and bottom of the wafers using mask # 1 and 2
2. Etching silicon layer down to the buried oxide layer using deep reactive ion etch (DRIE)
3. Evaporating gold on device side and bonding of the two mirror-symmetric halves of the components
4. Etching of the bottom of the wafers and releasing the final components

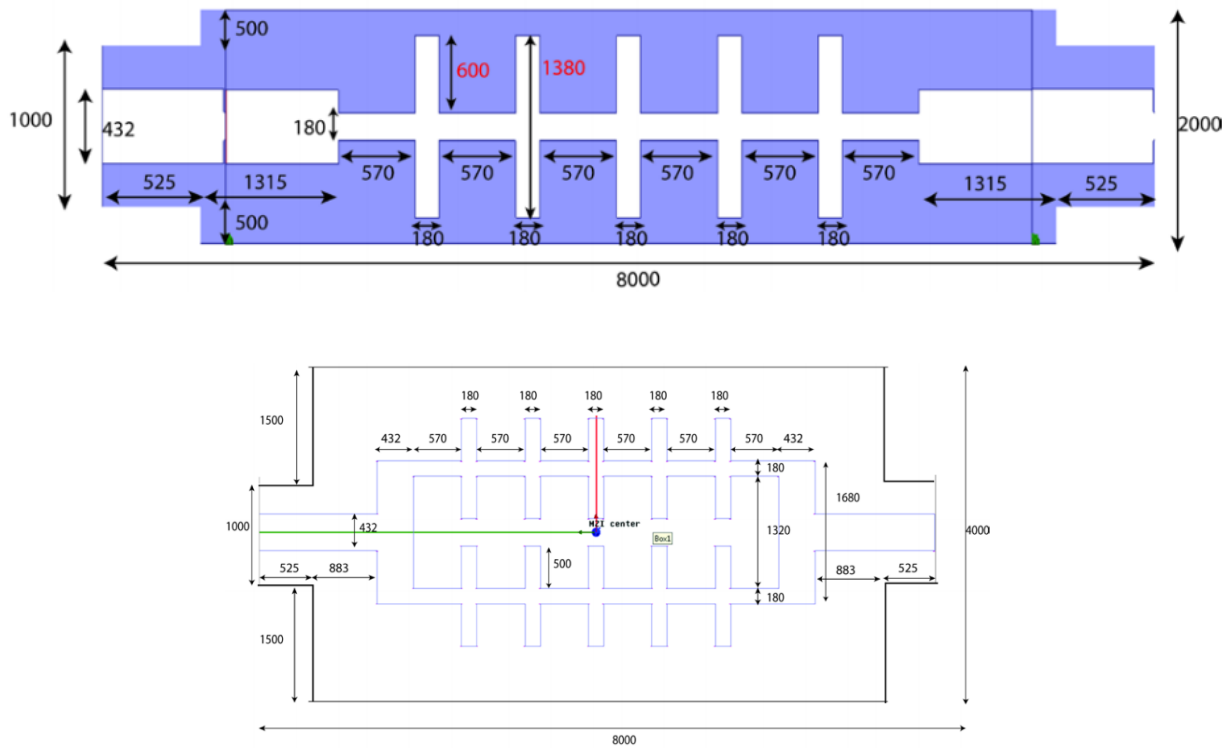


Fig. 18 Schematic view of SSPP waveguide with five periods of resonators and its corresponding MZI structure. Their dimensions are shown inside the figures.

More detail steps in the fabrication process are shown in Fig. 19. The thickness of device side is $431\mu\text{m}$ and the handle side is $250\mu\text{m}$ thick, the silicon oxide layer in the middle is $0.5\mu\text{m}$ thick and both sides are polished with $1\mu\text{m}$ silicon oxide. First, the device sides of two bare polished

SOI wafers are coated with thin layer ($3\mu\text{m}$) of photoresist. Fig. 19(b) shows the process. After coating the device sides with photoresist they are patterned with mask #1 and are developed. Fig. 19(d) shows the schematic view of mask #1, which includes different kinds of SSPP waveguides and different MZI structures. The photoresist that is used for patterning is SPR220. The SPR220 is a positive, general-purpose, multi-wavelength resist designed to cover wide range of film thickness from $1\mu\text{m}$ to $30\mu\text{m}$ with single coat process. For exposing the structure the MA/BA6 in LNF (Lurie nanofabrication facility) has been used. This device is a contact mask aligner and it is capable to pattern the structures as small as $2\mu\text{m}$. It uses a UV power supply that is calibrated to 20 mW/cm^2 at 405 nm . To have sharp pattern on the photoresist the exposure time should be defined accurately. After doing several attempts the optimized exposure time find to be 17sec.

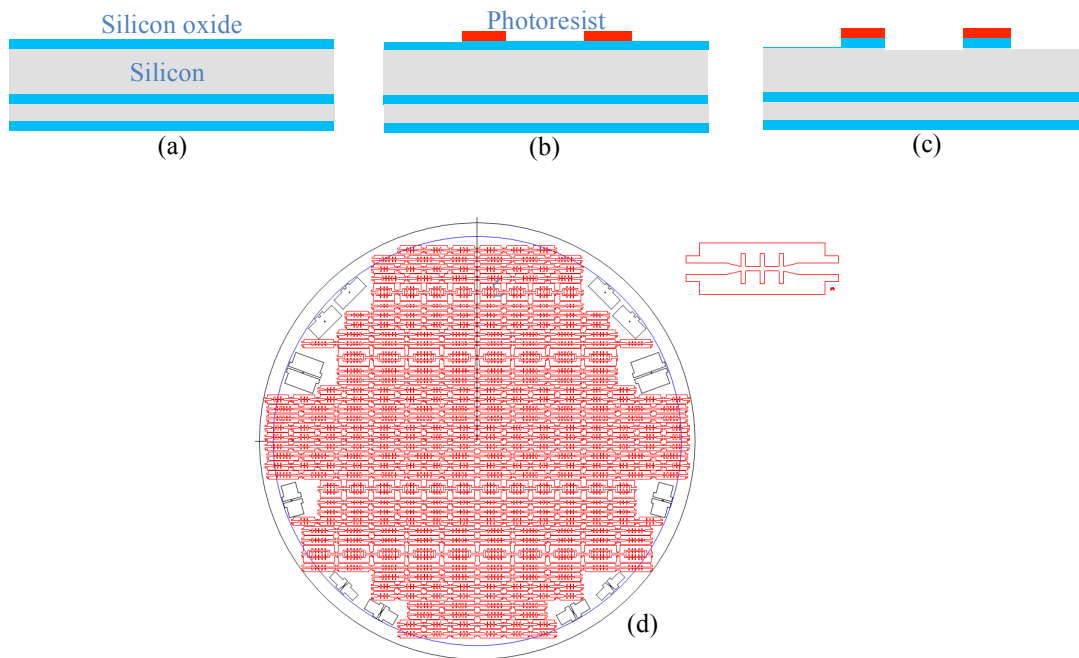


Fig. 19. (a) Bare SOI wafer, thickness of the device side is $431\mu\text{m}$ and the handle side is $250\mu\text{m}$ thick, the silicon oxide layer in the middle is $0.5\mu\text{m}$ thick. (b) Coating with $3\mu\text{m}$ of SPR220 photoresist and patterning. (c) Etching silicon oxide. (d) Schematic view of mask #1.

The next step is to etch the $1\mu\text{m}$ silicon oxide on top of the wafers until the buried silicon layer is exposed. Fig. 19(c) shows the schematic of process. To etch the silicon oxide layer reactive-ion etching (RIE) technique is used. The recipe's name for this process is "mnf-nitride1". This recipe etches the silicon oxide at a rate of 1200 Angstrom per minute. We have $1\mu\text{m}$ of oxide then the total time should be around 8 minutes. To make sure that the oxide is etched all the way the etching time set to 10 minutes. This results in etch a little bit of the silicon layer, but does not matter, as we will etch the silicon layer later.

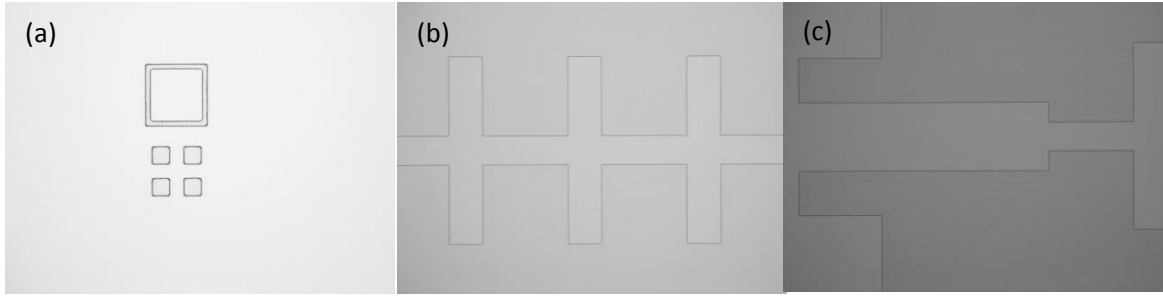


Fig. 20 (a-c) Photo of the handle side of wafers after RIE etching. (a) The alignment mark on the front side is shown. This sign is used to pattern the backside in alignment with the front side

After that, the two wafers are stripped from remaining photoresist using solvent or RF plasma stripper. To have cleaner surface, at first we used acetone to strip the photoresist and then RF plasma is used to remove all remaining dirt on the surface. At the next step, the handle side of these two wafers are patterned using the mask #2, after developing; the $1\mu\text{m}$ silicon oxide on bottom of the wafers is etched down to the buried silicon layer. Fig. 21(a)-(b) shows these steps. As the thickness of the oxide and photoresist on backside of the wafers are the same as front side all the timings and processes are the same as the front side. The next step is etching the silicon on the device side. Fig. 21(c) shows the schematic of this process.

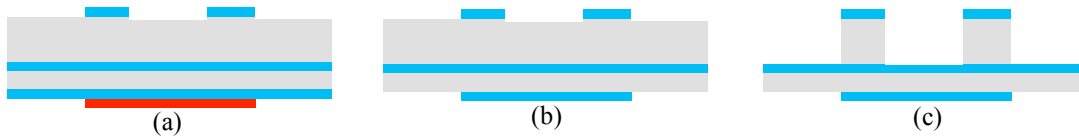


Fig. 21. (a) Coating the back side with $3\mu\text{m}$ of SPR220 photoresist and patterning the back side. (b) Etching silicon oxide at back side using RIE technique. (c) Etching the silicon layer using DRIE technique.

To etch the silicon, the deep reactive-ion etching (DRIE) technique is used to get highly accurate dimensions. This device helps us to etch deep inside the silicon with low undercut and high aspect ratio. The device name in the LNF is Pegasus. It is a powerful etch tool that has 6kW radio frequency power inductively coupled plasma. The reacting gases (SF_6) are pumped by a huge turbo pump at several Liter flow rate. The recipe number 2 in the Pegasus device is used for DRIE. This recipe has high selectivity between silicon oxide and silicon with respectively high etch rate. The etch rate is a function of the open area of the structure, then for each specific pattern on the mask we need to find the etching rate. To this purpose, at first the wafer is etched for 5 minutes then the depth of etch is measured. Finally we found that, this recipe for this specific design etches the silicon at rate of $10\mu\text{m}$ per minutes. And the total time to etch the silicon down to the buried silicon oxide in the middle is 43 minutes. To make sure there is no silicon underneath of the grooves, the etching time is set to 46 minutes. Fig. 22(a-c) shows the sample at different time slots during DRIE process. Fig. 22(d) shows the wafer after the DRIE is done on the front side.

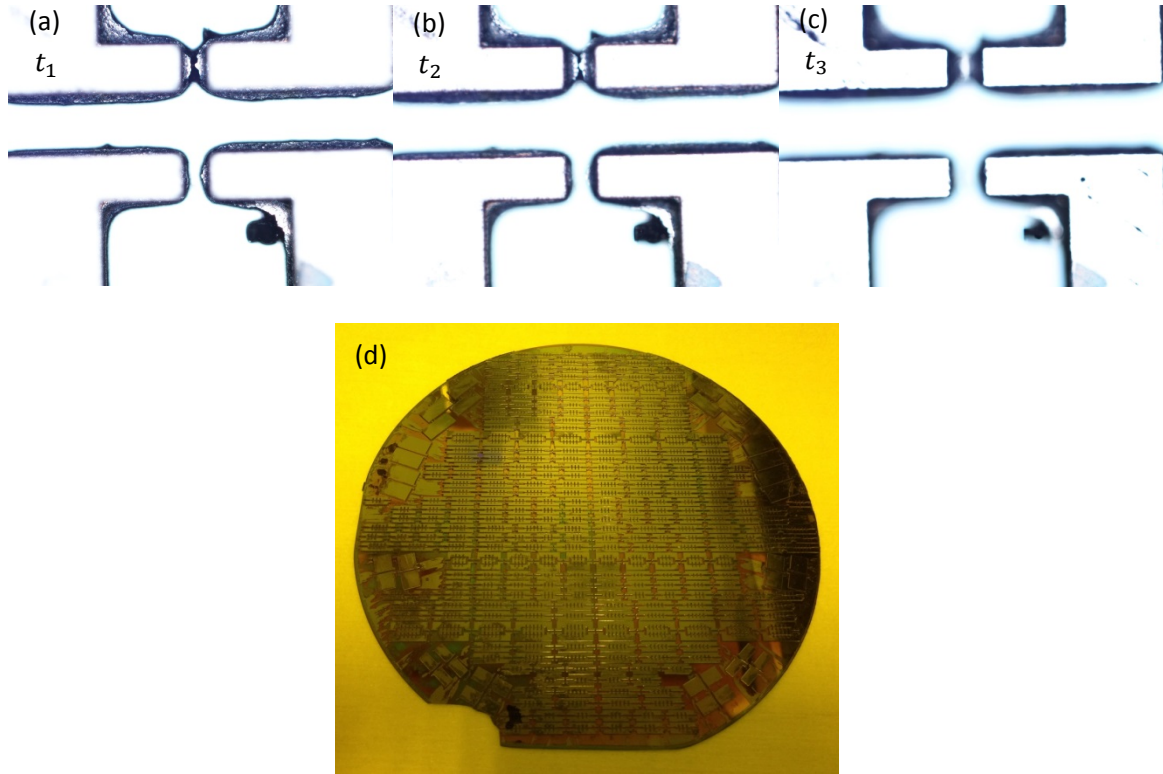


Fig. 22 (a-c) photograph of sample during DRIE at different time slots. ($t_3 > t_2 > t_1$) (d) photo of wafer after DRIE is done on the front side.

After etching the silicon, we need to deposit gold on the device side. To this purpose the physical vapor deposition (PVD) technique is used. After the DRIE, there is a thin layer of Teflon on the surface of the structure especially on the waveguide's and groove's walls. Then before doing any further process we need to get rid of this layer. To remove Teflon the plasma stripper is used.

To avoid silicon diffusion into gold which results in a lossy alloy in microwave to THz frequencies, we can deposit a thin layer ($0.5\mu m$) of silicon oxide before the gold layer deposition takes place. Another substitution to silicon oxide could be chrome. Chrome increases the adhesion of gold to the surface of our structure as the gold adhesion to the silicon and silicon oxide is too weak and during the process can be came off the surface. In the first attempt the most portion of the gold was deposited on the bottom of the waveguide and a very thin layer of it was on the walls, this happened as a result of long distance between silicon wafers and gold evaporator source and small dimension of gold evaporator source. To fix this problem, the new PVD equipment is used in which the distance between wafers and gold evaporator sources is much closer and the gold source is also extended. This results in more uniform deposition of gold on both bottom and walls. Fig. 23(a) shows the process.

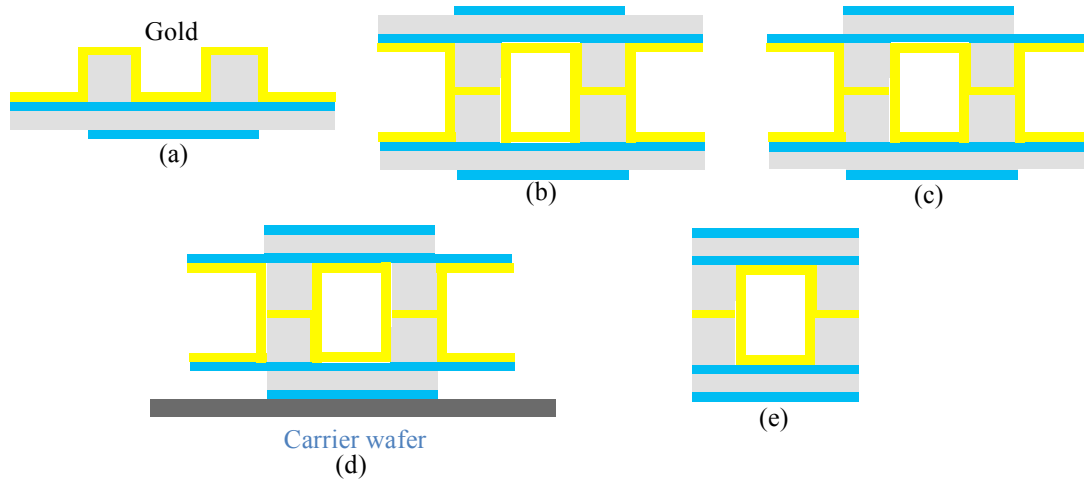


Fig. 23. (a) Gold deposition. (a) Bonding. (a) Etching the silicon at the top of wafer. (d) Mounting to carrier wafer (e) etching the remaining silicon.

As shown in Fig. 23(b), the two wafers are aligned and bonded together. For the initial bonding process, the force set to 2500 N and temperature to 390 °C. The bonding only takes place at the outer edge of wafers and the components easy to split up when we separate all the parts. Fig. 24 shows the last fabricated components after gold evaporating and before bonding. In these photos the grooves are etched perfectly and the structure has clean and sharp edges.

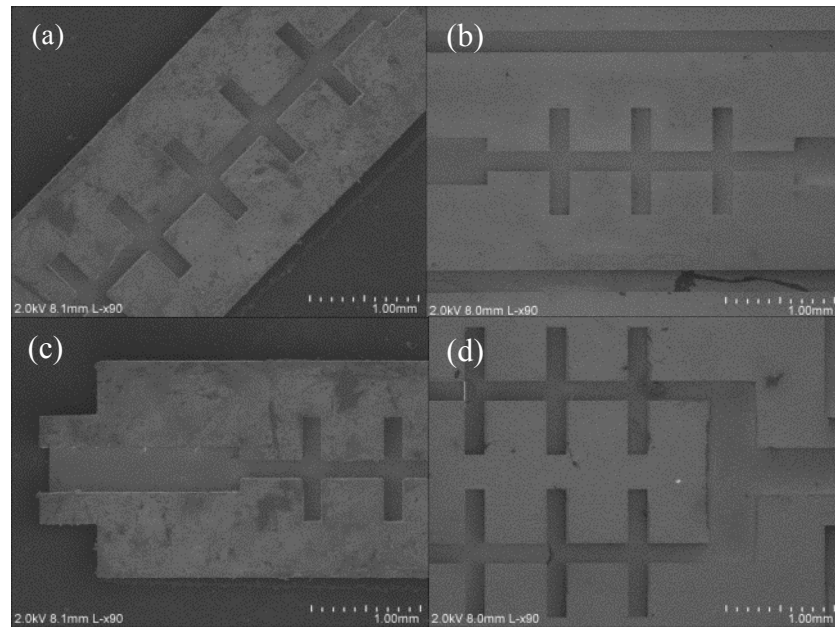


Fig. 24(a) SSPP waveguide with five corrugations. (b) SSPP waveguide with 3 corrugations. (c) SSPP waveguide and the WR3 feed point. (d) Mach-zehnder interferometer.

To overcome the bonding problem, the thickness of gold is increased from $0.5\mu\text{m}$ to $1\mu\text{m}$ so that we have more gold to melt and bond the wafers, while the temperature is increased to 430°C and the force to 16000 N . With these parameters the output was better and we have reached a yield of 60% satisfactory parts out of the total number in the batch. The excessive force results in cracks in certain components. Also, increasing the thickness of gold can increase the output yield, but it can cause the extra melted gold to move into the structure and cause some problem. Then there is an optimum thickness for the gold deposition. We plan to increase the temperature and decrease the force in our next batches of fabrication to find the optimized parameters for bonding recipe. The final step is to etch the top and bottom of bonded wafers. Fig. 23(c)-(d) show the schematic of the process. At first one side is etched until the buried silicon oxide layer. The recipe number is again number 2. The etch rate is calculated and is approximately the same as the front side. The time is set to 25 minutes to completely etch all the silicon between the devices. Plasma etch creates heat, the chamber in Pegasus is 120°C , and the etch reaction is exothermic. As a result, the wafer gets heated to $50\text{--}55^\circ\text{C}$ during processing, if well mounted. As the structure is made out of two bonded wafers the heat can cause uneven expansion in the structure and results in some crack. Then it is better not to etch the entire wafer at the same time. We did this process at 4 steps and each step set to 6 minutes. At the next step, it is flipped and mounted to a carrier wafer and the other side is etched to the silicon oxide layer. To mount the wafer to the carrier, crystal bond is used and the process is done under the vacuum condition. If there is any air trapped inside the samples and carrier wafer, when we put it in the Pegasus to do DRIE it can result in cracking the samples. At the end, we need to release the samples from the carrier wafer. To separate the parts we put them in hot water (80°C) then the crystal bonds dissolved in water and final components release. As the remaining silicon oxide in the middle is just $1\mu\text{m}$, it can easily break and all the parts release in the water. Fig. 24 shows samples after releasing from the carrier wafer.



Fig. 24 fabricated sample after releasing from the carrier wafer.

Fig. 25 (b, c) shows the final samples after being released from the carrier wafer and attached to the flanges. As mentioned earlier to release the final samples we put them in the hot water at 80°C to dissolve crystal bond into the water. After rinsing and drying all the samples there could be some remaining of crystal bond inside the waveguides especially inside the grooves. In order to clean the inside of the samples from any remaining crystal bond the plasma stripper is used again. The samples are heated up to 80°C for 6 minutes in vacuum. Fig. 25(a) shows some sample waveguides in which their top and bottom parts of them are separated.

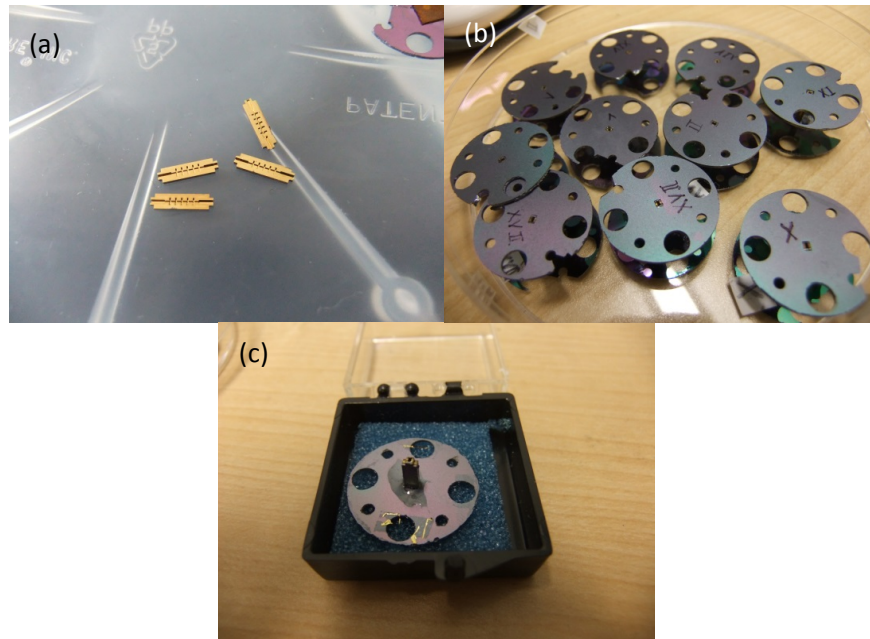


Fig. 25(a) Halves of SSPP waveguide with five corrugations after evaporating gold on the silicon . (b) Final SSPP waveguide after bonding and releasing from the carrier wafer (b, c) SSPP waveguide and the WR3 feed point. Connected to the flanges.

The flanges are used to connect the fabricated samples to the network analyzer for the purpose of measurement. They are designed to connect to the WR-3 standard port. The flanges are fabricated using bare silicon wafer. The thickness is not important. To fabricate these flanges we used a silicon wafer covered by thin layer of silicon oxide. First a layer of SPR220 photoresist with the thickness of $3\mu m$ is spanned on the silicon oxide layer. Then the photoresist is patterned with the mask. Fig. 26 shows the schematic design of the mask for making flanges. The exposure time set to 17 sec. As the dimensions are big and the accuracy for making the flange is not critical, we do not do any process to find the exposure time. After that, the RIE etch is used to etch the silicon oxide. Again the same timing as previous is used. Then the photoresist is stripped using acetone. The next step is to mount the wafer to the carrier wafer using crystal bond. Then the DRIE method is used to etch the silicon layer all the way. Finally by putting the samples in the hot water they all separated from carrier wafer.

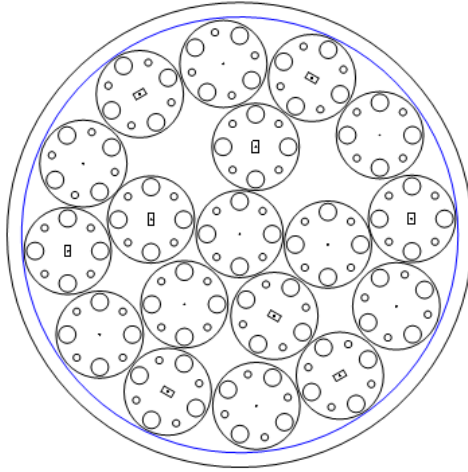


Fig. 26 The schematic design of the mask for making flanges.

2. Future work for fabrication:

As we mentioned earlier, in the first batch, gold evaporating technique was used for deposition. This result in unevenness of gold deposition on the groove's wall then the lack of metal on the surface of the silicon waveguide will introduce serious loss to the device. It will also break the boundary conditions under which the SSPP resonance would occur. To have better deposition on the walls gold sputtering should be used. We used the sputtering technique for the last batch but more fabrications need to be done to get the best result. This will make approximately even gold deposition on the groove's wall. Also the bonding process is another critical step in our fabrication recipe. Right now the yield 60% of the total number of samples. To have the better bonding we need to increase the gold thickness inside the waveguide but increasing the gold thickness results in some unevenness in the bonded edges. We need to decrease the gold thickness a little bit and increase the temperature and pressure during bonding. This requires several runs on different batches to find the proper gold thickness, bonding temperature and pressure. The other problem is the DRIE etch. During the silicon etch some small holes appear on the silicon surface. Fig. 27 shows the photo of some samples during DRIE.

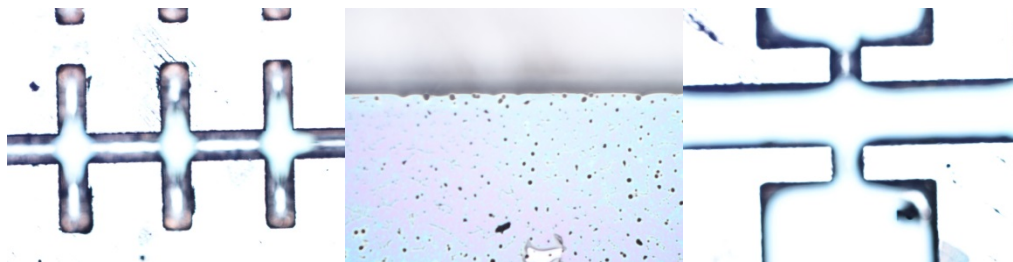


Fig. 27 Photo of the samples during the DRIE etch.

As can be seen, during the silicon etching process, some small holes appear on the silicon surface. These holes result in uneven surface, and ultimately will generate loss in the THz

transmission. Some of these defects can appear as a result of dirt on the surface of the wafer. To overcome this dirt we need to do more cleaning process before the DRIE process and doing plasma etch to completely cleaning the silicon surface from any photoresist or organic compound that can prevent from silicon etch.

Fig. 28 shows SEM image of some components right after the DRIE. If there is any unwanted silicon on the wafer like Fig. 28 (b) we can do DRIE for a longer time to etch them all the way. But increasing the time can result in undercut and even damage to the oxide layer. To get rid of these problems we need to work on DRIE recipe and oxygen plasma etch.

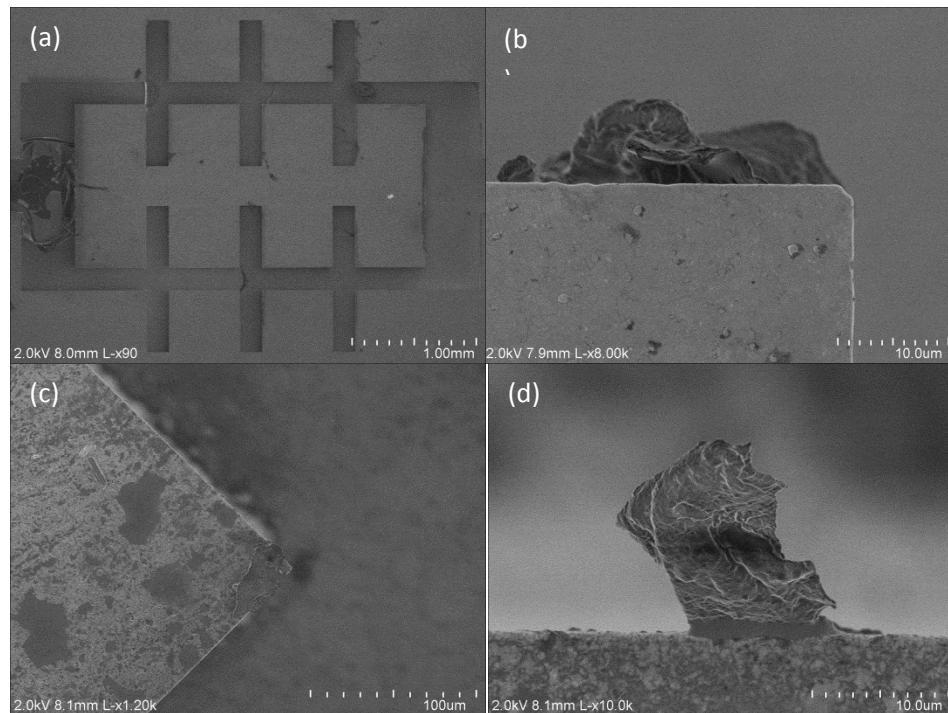


Fig. 28 SEM image of damaged fabricated samples.

The other problem is the uneven etch of the silicon. The recipe that is used for the DRIE, etches the silicon at high rate and etches the silicon oxide at very slower rate. But the etch rate is not equal all over the wafer and also it changes by the temperature. Our observation shows the etch rate at the center of the wafer is higher than the corners. And at some places the oxide layer etches completely that results in some damaged samples. To decrease the etch rate of the silicon oxide we should work on the DRIE recipe to increase its selectivity between silicon and silicon oxide. Also to reduce the heat effect on the wafer we can use the same solution that we did for the DRIE of backside. We can divide the etch time and doing silicon etch in several steps to let the wafer cools down.

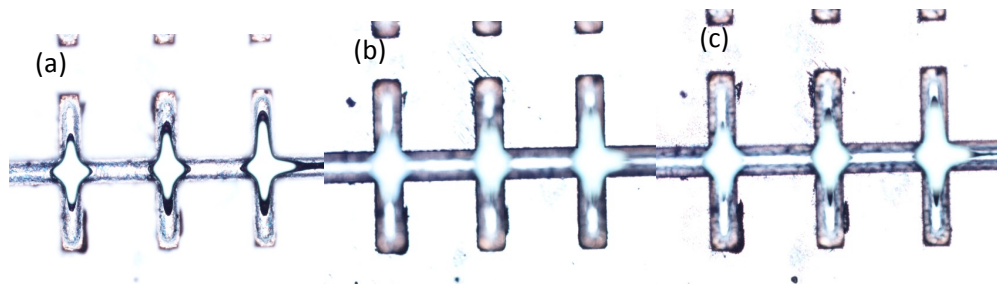


Fig. 29 photo of sample during DRIE, as shown the grooves edges are not sharp and in some cases the silicon oxide is etched.

Note: This research was made possible through the funding of two grants. "Plamronics for Biomolecular Sensors and THz Metamaterial Waveguides", and "Near and Far-Field Interfaces to DNA-Guided Nanostructures from RF to Lightwave: Exploiting the Spectrum"